BASIC RESEARCH GRANT (Final report*)

BRG 5180010

Development of Magnetic Nano Particles for Biomedical Applications: Ferrite Doped Hydroxyapatite Nanoparticles for Hyperthermia Treatment of Cancer.

*The Bank Account for the grant was opened on June 25, 2008, with funds from Thailand Research Fund (TRF) deposited on July 22, 2008. The second installment of the funds was deposited in the bank account on April 3, 2009. The project was completed on October 3, 2009.

Researchers:

Principle Investigator: **Professor Dr. I-Ming Tang, Ph.D.**

นาย อิ มิง ถัง

Other Investigators: **Dr. Jose H. Hodak, Ph.D.**

นาย โจเซ่ โฮดัก

Miss Nattasamon Petchsang, M.Sc.

นางสาว ณัฐสมน เพชรแสง

Miss Ketvalee Treegate

นางสาว เกศวลี ตรีเกตุ

Project Duration: One year.

Objectives

1. To fabricate iron doped hydroxyapatite nano particles of various sizes.
2. To determine which form of iron should be introduced into the composite nano particles, i.e., in the form of iron itself or as one of the components of some spinel ferrite, e.g., Fe_3O_4, $CoFe_2O_4$, $MnFe_2O_4$ or $NiFe_2O_4$.
3. To determine whether under what conditions can the magnetic nano particles be heated up to the desired temperatures.
4. To see whether magnetic nano-particles can be moved in the blood into the vicinity of the tumor by placing strong magnets close to the tumor and whether

they can be removed from the body by passing the blood through a shunt surrounded by a magnet.

5. To see whether other materials can be used to form the shell.

Research Report

A. Fabricate iron doped hydroxyapatite nano particles of various sizes.

It was reported in the mid report that the paper, co authored by N. Petchsang, W. Pon-On, J.H. Hodak, I.M. Tang,

"*Magnetnic Properties of Co-Ferrite Nano-particles having a Core/Shell Structure."*

was published in Journal of Magnetism and Magnetic Materials **321**, 1990 (2009).

Paper can be found in Appendix A 2

B. To determine which form of iron should be introduced into the composite nano particles, i.e., in the form of iron itself or as one of the components of some spinel ferrite, e.g., Fe_3O_4, $CoFe_2O_4$, $MnFe_2O_4$ or $NiFe_2O_4$.

B .1 A new method (chemical) for fabricating ferrite doped hydroxyapatite nano particles is now introduced.

Method for synthesis ferrites

1. Mixed $FeCl_3$ and one of these chemical $FeCl_2$, $CoCl_2$, $NiCl_2$, $MnCl_2$ in water with HCL 0.85 ml.
2. Add drop wise in NaOH 1.5 M. Then the precipitation was black.
3. Wash the precipitation with water at lease 3 times by centrifuge.
4. 0.01M HCL was add in the precipitation.
5. Wash again by water and ethanol.
6. Measured samples by TEM and Mossbauer

Result of fabricating different ferrites using the new method

1. TEM images.

i. $CoFe_2O_4$

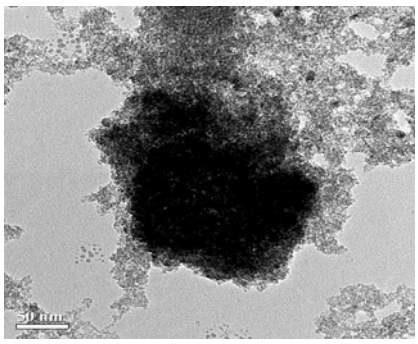

ii. MnFe2O4

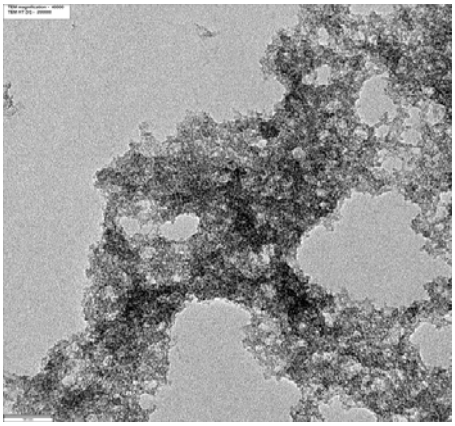

iii. NiFe2O4

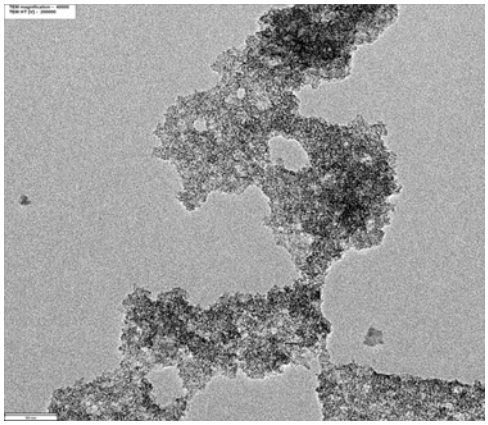

iv. Fe3O4

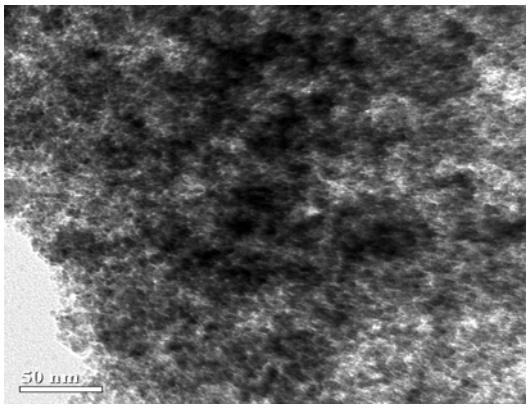

Inspecting the TEM images, we see no differences between them. However when the Mossbauer measurements are used to study the hyperfine fields with the different spinel ferrites, we see that there are differences between them.

2 Mossbauer Spectrums.

i. $CoFe_2O_4$

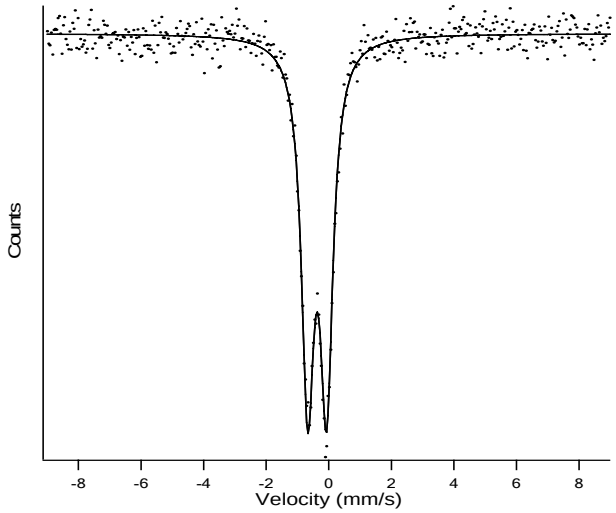

Quadrupole splitting	=	0.604
Isomer shift	=	-0.371
Outer width	=	0.49

---

iii. $MnFe_2O_4$

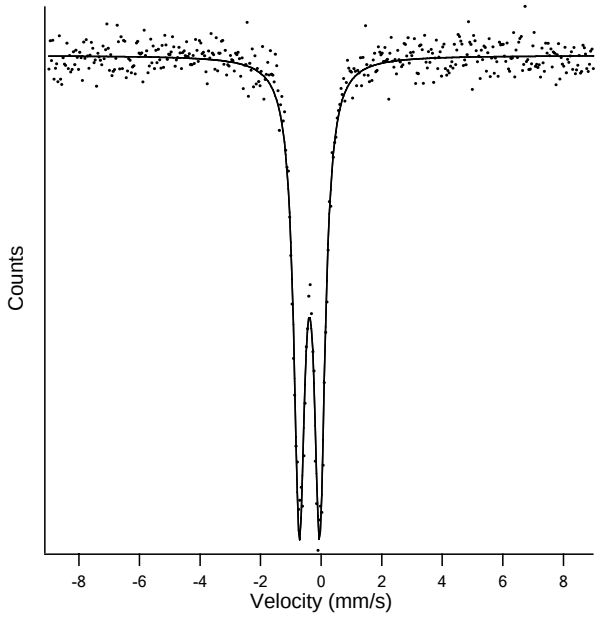

Quadrupole splitting	=	0.671
Isomer shift	=	-0.385
Outer width	=	0.434

iii. $NiFe_2O_4$

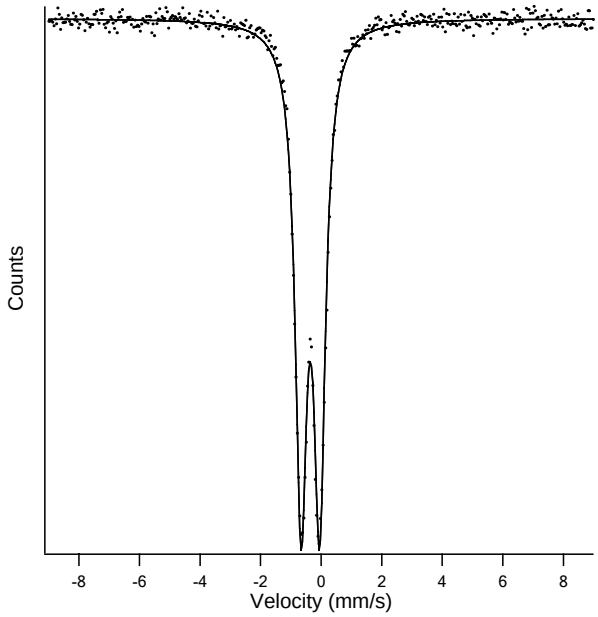

Quadrupole splitting	=	0.616
Isomer shift	=	-0.354
Outer width	=	0.446

iv. Fe_3O_4

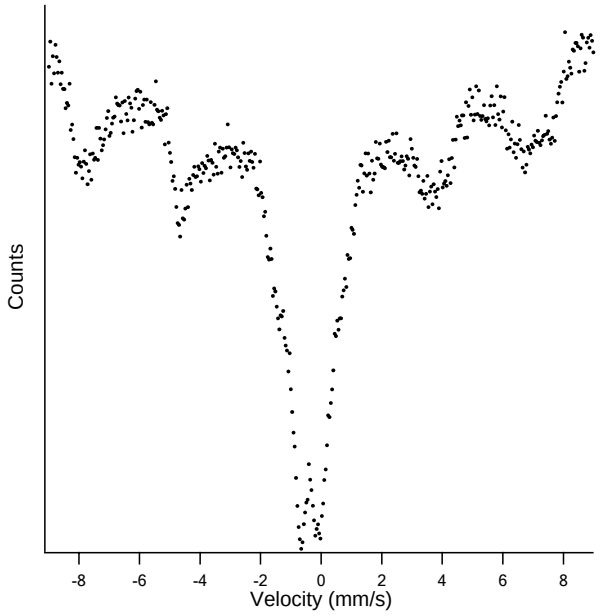

As is clearly evident, the Mossbauer spectra of Fe_3O_4 is completely different from those of $CoFe_2O_4$, $MnFe_2O_4$ and $NiFe_2O_4$. The difference can be easily explained by the simple fact that the Fe^{2+} ion has a higher magnetic moment than do the other divalent ions have. Therefore the exchange interaction in Fe_3O_4 is larger than those in the other three. This means that the hyperfine field in Fe_3O_4 is stronger than those in the other three again. Because the nano particles fabricated are extremely small, the long range ordering in these particles are weak. In these Fe_3O_4 nano particles, the hyperfine field strengths are still strong enough to overcome the disordering effects of the temperature (room temperature) and so the nano particles are still ferromagnetic. In the other nano size spinel ferrite particles, the hyperfine field strengths are small so that the disordering energy of the thermal noise can overcome the long range ordering arising from the hyperfine field interaction. This results in these nanoparticles being paramagnetic. The doublet lines seen in their Mossbauer spectrums are signatures of the paramagnetic state.

B.2 Borohydride reduction of ferrous ions revisited: a complex and versatile route to ferromagnetic nanoparticles; Controllable pathway to alpha-iron magnetic nanoparticles.

Synthesis method.:

An aqueous solution of iron II sulfate (0.4 ml) was quickly added (within one second) with a syringe to a vigorously stirred aqueous solution of $NaBH_4$ freshly prepared and containing citric acid or oxalic acid as a stabilizer. The borohydride solution had a concentration that varied between 4.4×10^{-6} and 1.6×10^{-3} mol/l and was thoroughly purged with argon for 30 min to remove any dissolved air. The injection of the iron containing solution caused a grey suspension to appear almost immediately. Magnetic stirring was avoided mainly to prevent magnetization of the products and also to avoid its agglutination on the magnetic bar.

Within 3 seconds of mixing the iron and the borohydride solutions, 400 ml of an argon-purged solution of tetraethyl orthosilicate in ethanol (4.5×10^{-5} Mol/l) was added via an addition funnel over a period of one minute with gentle stirring under an argon stream. The resulting pale grey suspension was allowed to stand for 20 minutes and the solid was collected by centrifugation at 10,000 RPM (10 min). The precipitate was washed 4 times with ethanol, and collected by centrifugation into a vial. The remaining ethanol was evaporated in a desiccator at room temperature.

Material Characterization

Transmission electron microscope specimens were prepared by diluting 0.02 ml of the suspension before the final centrifugation step to 0.2 ml with ethanol. One droplet of the resulting solution was placed on a carbon/formvar cooper grid (SPI 200 Mesh). A Jeolab Model 2010 transmission electron microscope was used for obtaining the microphotographs and electron diffraction patterns.

Specimens for the Mössbauer experiments were prepared by collecting all of the dry sample in a circular cutout on a piece of paper (6 mm diameter, 0.1 mm thick) which

was covered by a thin waxed paper and closed with transparent adhesive tape (Scotch tape). The Mössbauer system was composed of a constant acceleration transducer (FAST COMTEC model 251 and controller MD351, an analog to digital converter model 2076 (Canberra) and a preamplifier Pas-2 (FAST COMTEC). The gamma source was an ^{57}Co in rhodium source, and the detector was a gas filled proportional counter model 45431 (LND INC). The velocity scale was calibrated using a 0.0125 mm thick iron foil (Goodfellow). Powder X-ray diffraction patterns were obtained in a Bruker Discovery D-8 diffractometer by completely transferring the dry sample to a zero background silicon plate. The calibration of the diffractometer was done using a quartz powder standard.

Results and discussion

The diffuse diffraction pattern in figure 1-a) is consistent with amorphous Fe_2B. Disappearing when the ratio $[BH_4^-]/[Fe^{+2}]$ is larger than ca. 100. In contrast to the pattern shown in figure 1-a), the diffraction patterns in figure 1-b) and c) are consistent with a mixture containing $\alpha - Fe$ and Fe_2B. The data in the lower panel of Fig. 1d) corresponds to $\alpha - Fe$ only. These results suggest that the reaction pathway can be changed by the BH_4^- / Fe^{+2} ratio. To investigate this more quantitatively we have measured the room temperature Mössbauer absorption spectra of the samples. Mössbauer spectra for the samples prepared at different $[BH_4^-]/[Fe^{+2}]$ ratios are shown in Figure 2. The spectra contain a sextet of bands indicating that the samples are ferromagnetic at room temperature. The lines become sharper and more intense when the synthesis is carried out at higher $[BH_4^-]/[Fe^{+2}]$ molar ratios. These spectra could not be fit to a single sextet with physically meaningful line widths. They therefore were tentatively treated as ternary mixtures with variable amounts of $\alpha - Fe$, Fe_2B and the paramagnetic iron oxide-hydroxide $\beta - FeOOH$. These materials were guessed at on the basis of known hyperfine field parameters and quadrupole moments for ^{57}Fe reported in the literature, Using this approach we successfully deconvolute the measured Mössbauer data into the 3 sub spectra as shown in figure 2 (cf. thin, dashed and, dash-dotted lines, (color online)). The goodness of the least-squares fit was judged by the reduced χ^2 of the sum of all sub spectra which is the envelope (figure 1 thick black line). The sub spectrum used to fit the broad sextet with low hyperfine field was composed of 20 sextets covering fixed hyperfine fields between 1 and 31 Tesla. The values for their quadrupole moments and isomer shift were also fixed. Amplitudes of all the sextets within the distribution were allowed to vary. The value of the isomer shift and average quadrupole splitting for the sextets in the distribution was found by fitting the broad peaks to a single sextet of variable width quadrupole splitting and isomer shift. The final fits also adjusted all the parameters for the narrow sextet with the exception of its quadrupole splitting. A sub spectrum showing a doublet is also present in the data, which can be fitted by adjusting the quadrupole splitting, the isomer shift the amplitude and line with. The fits yielded a component with an average hyperfine field of 33.250 ± 0.001 T with zero quadrupole splitting thus, confirming the presence of $\alpha - Fe$ in our particles. The broad sextet is character is of a distribution of hyperfine fields with a maximum at 27.90 ± 0.01 T. The relative amount of the distribution decreases as the $[BH_4^-]/[Fe^{+2}]$ molar ratio increases. In all our samples

there is always some contribution from an amorphous phase. The relative areas of the sub spectra are proportional to the number of ^{57}Fe atoms contributing to it. Therefore, quantitative information about the composition can be obtained from the fits to the Mossbauer data. Figure 3 shows the variation of the amplitude of the distribution and that of the narrow sextet as a function of the $[BH_4^-]/[Fe^{+2}]$ molar ratio. The yield of Fe_2B is reduced to ca. 30% when $[BH_4^-]/[Fe^{+2}] \approx 100$.

We believe that the formation of the iron most likely occurred by conversion of the Fe_2B by the catalytic decomposition of BH_4^-. To test this hypothesis we carried out experiments using molar ratio $[BH_4^-]/[Fe^{+2}] = 10$ (cf. Fig. 1a)) and injected the iron solution in two steps. First 0.1 ml (3×10^{-5} moles of Fe^{+2}) was introduced followed by with a waiting period of 10 seconds and then the remaining 0.3 ml (3×10^{-5} moles) was quickly added. Upon the first injection, a grey precipitate appeared which lead to the evolution of some gas during the waiting time. The addition of the second fraction of the iron solution only produced a darker suspension. After passivation with silica and isolation a black powder resulted which was seem to be composed of a broad size distribution of particles. Figure 4(a-b) shows the TEM microphotograph of the particles and the corresponding electron diffraction pattern. The particles appear to have similar sizes and morphologies as seen in Fig. 1b-d. The electron diffraction data and the powder X-ray diffraction pattern in Fig 4c clearly show reflections consistent with the bcc plane families $\{110\}(2\theta = 44.87^\circ)$, $\{220\}(2\theta = 65.32^\circ)$ and $\{112\}(2\theta = 82.56^\circ)$ in $\alpha - Fe$. The Mössbauer spectrum of the sample is shown in Figure 4d). In contrast with the spectrum seen in Fig. 2a), narrow peaks are present in the spectrum shown in Fig. 4d. The data was fit to the same ternary mixture as done for Figure 2. The most striking feature of this data is that a narrow sextet with a hyperfine field consistent with $\alpha - Fe$ is now evident for samples prepared with low $[BH_4^-]/[Fe^{+2}]$ ratio. In particular, the Mössbauer results are comparable to those obtained at considerably higher $[BH_4^-]/[Fe^{+2}]$ molar ratios which support our hypothesis that the yield of zerovalent iron is connected to a catalytic reaction taking place on the Fe_2B surface.

To explain the formation of $\alpha - Fe$,Klabunde proposed a mechanism for the reaction of aqua-complexes of iron with borohydride under anaerobic conditions. In his mechanism, an intermediate iron borohydride-aqua-complex is formed which undergoes electron transfer from the borohydride ligand to the ferrous nucleus,

$$[Fe(H_2O)_6]^{2+} \rightarrow [(H_2O)_5 FeOH]^{+} \quad \text{(a)}$$

$$[(H_2O)_5 FeOH]^{+} + H^{+} + BH_4^{-} \rightarrow [(H_2O)_5 FeO(BH_3)H] + H_2 \quad \text{(b)}$$

$$[(H_2O)_5 FeO(BH_3)H] + BH_4^{-} \rightarrow \frac{1}{2} H_2 + BH_3 + [(H_2O)_5 Fe(OHBH_3)] \quad \text{(c)}$$

$$[(H_2O)_5 Fe(OHBH_3)] \rightarrow Fe^0 + \frac{1}{2} H_2 + HOBH_2 + 5H_2O \quad \text{(d)} \quad (3)$$

$$HOBH_2 + 2H_2O \rightarrow B(OH)_3 + 2H_2 \quad \text{(e)}$$

$$BH_3 + 3H_2O \rightarrow B(OH)_3 + 3H_2 \quad \text{(f)}$$

$$[Fe(H_2O)_6]^{2+} + 2BH_4^{-} \rightarrow Fe^0 + 7H_2 + 2B(OH)_3. \quad \text{(g)}$$

This mechanism was used to explain the products of reactions by addition of the iron solution to solid sodium borohydride. The vastly different mixing conditions used in our experiments may cause a departure from this mechanism. However, it provides invaluable guidance towards understanding this system. The dependence of the product with the $[BH_4^-]/[Fe^{+2}]$ ratio can be explained by this reaction pathway by the step (c) in Eqn. 3. This reaction would occur faster at higher BH_4^- concentrations and lead to reduction of the product of step (b) by the second BH_4^- molecule, thus producing the higher yield of $\alpha - Fe$.

It is however not clear according to this scheme, how the two-step addition of the iron solution would increase the yield of zerovalent iron. Since the first addition occurs under an effective $[BH_4^-]/[Fe^{+2}]$ equal to 40, it would be expected that $\alpha - Fe$ would result. However the second addition of the iron solution occurs under a ratio $[BH_4^-]/[Fe^{+2}]$ smaller than 10. The expectation is that less than 25% of the iron should be converted to $\alpha - Fe$ and the rest would appear as Fe_2B. In contrast, the sample shown in Fig. 4 contains 46% of $\alpha - Fe$ and only 35% of Fe_2B. Furthermore, addition of a few droplets of the iron solution followed by the complete addition a few tens of seconds latter can cause the formation of significant yields of $\alpha - Fe$ even at a $[BH_4^-]/[Fe^{+2}]$ ratio equal to 10. We speculate that the iron added during the second addition quickly forms Fe_2B and $\alpha - Fe$ particles which adsorb BH_4^-. Hydrogen and borate are generated by catalytic decomposition of borohydride according to Eqn. (2). The direct reduction of Fe^{+2} to $\alpha - Fe$ by hydrogen is thermodynamically unfavorable at the conditions used in our experiments. A likely mechanism is therefore the reaction

$$Fe(BO_2)_2 + 2Fe_2B \rightarrow 5Fe(s) + 2B_2O_x \xrightarrow{Oxygen} 5Fe(s) + 2B_2O_3 \quad (4)$$

The last step in the reaction is presumed to occur when the sample is exposed to air. When waiting periods longer than 20 seconds between the iron injections are used, the yield of $\alpha - Fe$ decreases and that for the paramagnetic oxide increases. We believe that this is due to reduction of the initially formed Fe_2B into iron and subsequent corrosion before the second addition occurs. We then interpret the results of Figs.1-2 as follows. At low $[BH_4^-]$ during the single iron addition not much borate can be formed because of the slow reaction and short reaction time. Thus, the main product

results to be Fe_2B. Under conditions of high [BH_4^-], borides are formed and carry the intermediate catalytic formation of H_2 and the $Fe(BO_2)_2$ which further reacts with Fe_2B, leading to the formation of $\alpha - Fe$ via Eqn 4. Under circumstances where the oxygen removal is incomplete, the formation of paramagnetic iron oxide-hydroxide $\beta - FeOOH$ occurs, which we assigned to the doublet sub-spectrum to this compound. This was readily verified by deliberately allowing air into the system during the reaction. This caused the quantitative conversion of the iron into a yellow precipitate. The effect of the stabilizing agent Citrate versus Oxalate and shape inducing effects

Citrate is often used in the preparation of nanoparticles for its stabilizing role. We have adopted this stabilizing agent based on the analogy of our synthesis with that of cobalt nanoparticles in aqueous medium using sodium borohydride as a reducing agent. In our syntheses the citric acid can be omitted with the penalty that the resulting nanoparticles have a much broader size distribution. It appears that citrate plays a role in determining the size of the particles. We tested this by varying the amount of citric acid used in the preparation. The results are shown in Figure 5. The histograms on the left panels of figure 6 clearly show that the mean diameter of the particles decreases from 75 nm to ca. 20 nm when the citrate concentration changes from 2×10^{-6} to 2×10^{-4} Mol/l which corresponds to a range of 0.005 to 0.5 in Citrate/iron molar ratio. These results are similar to those found in the synthesis of cobalt nanoparticles via a reduction with sodium borohydride. The size follows a nearly linear trend with the logarithm of the citrate/iron concentration ratio. The reduction of the size of the particles may be related to the binding citrate ions to iron atoms on the surface of primary particles, thus preventing their clustering and aggregation into larger structures.

Figure Captions

Figure 1
Transmission electron micrographs (top panel) and selected area electron diffraction patterns (bottom panels) of the particles resulting from borohydride reaction with ferrous ions for varying molar ratio BH_4^- / Fe^{+2}, from a) to d) 10, 33, 100 and 370. The BCC zone axes used in panels b)-d) are [210], [311] and [100] respectively.

Figure 2
Mossbauer spectra for the products shown in figure 1 (color online). The spectra are fit to a Zeeman-split alpha iron sextet (red dash-doted lines), a distribution of Zeeman split sub spectra with hyperfine fields in the 1-32 T range (solid blue lines) and a quadrupole split sub spectrum (green dashed lines). The black solid lines are the fit envelopes.

Figure 3
Variation of the partial absorption intensities of Fe_2B and $\alpha - Fe$ Mosbauer with BH_4^- / Fe^{+2} molar ratio.

Figure 4
Particles obtained by adding the iron solution in two separate aliquots (color online): a) transmission electron microphotograph. The insert is a diffraction pattern from a large number of particles contained in the field of view; b), selected area diffraction pattern from a small number of particles; c), powder X-ray diffraction, and, d) Mossbauer

spectrum (dots). The spectrum contains a Zeeman-split $\alpha - Fe$ sextet (red dash-doted line), a distribution of Zeeman split sub spectra with hyperfine fields in the 1-32 T range (solid blue line) and a quadrupole split sub spectrum (green dashed line).

Figure 5
Variation of the particle sizes with the concentration of colloid stabilizer; citric acid (left), oxalic acid (right). The insert show the mean diameter estimated from fitting the size distributions for citric acid (solid line) and oxalic acid (dashed line). The error bars correspond to the standard deviation of the distribution.

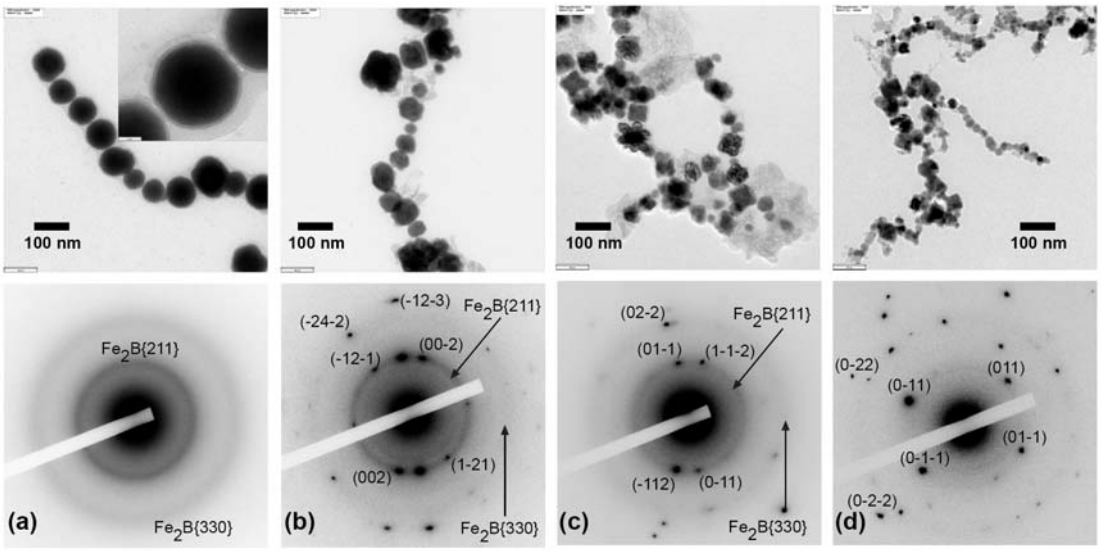

Figure 1

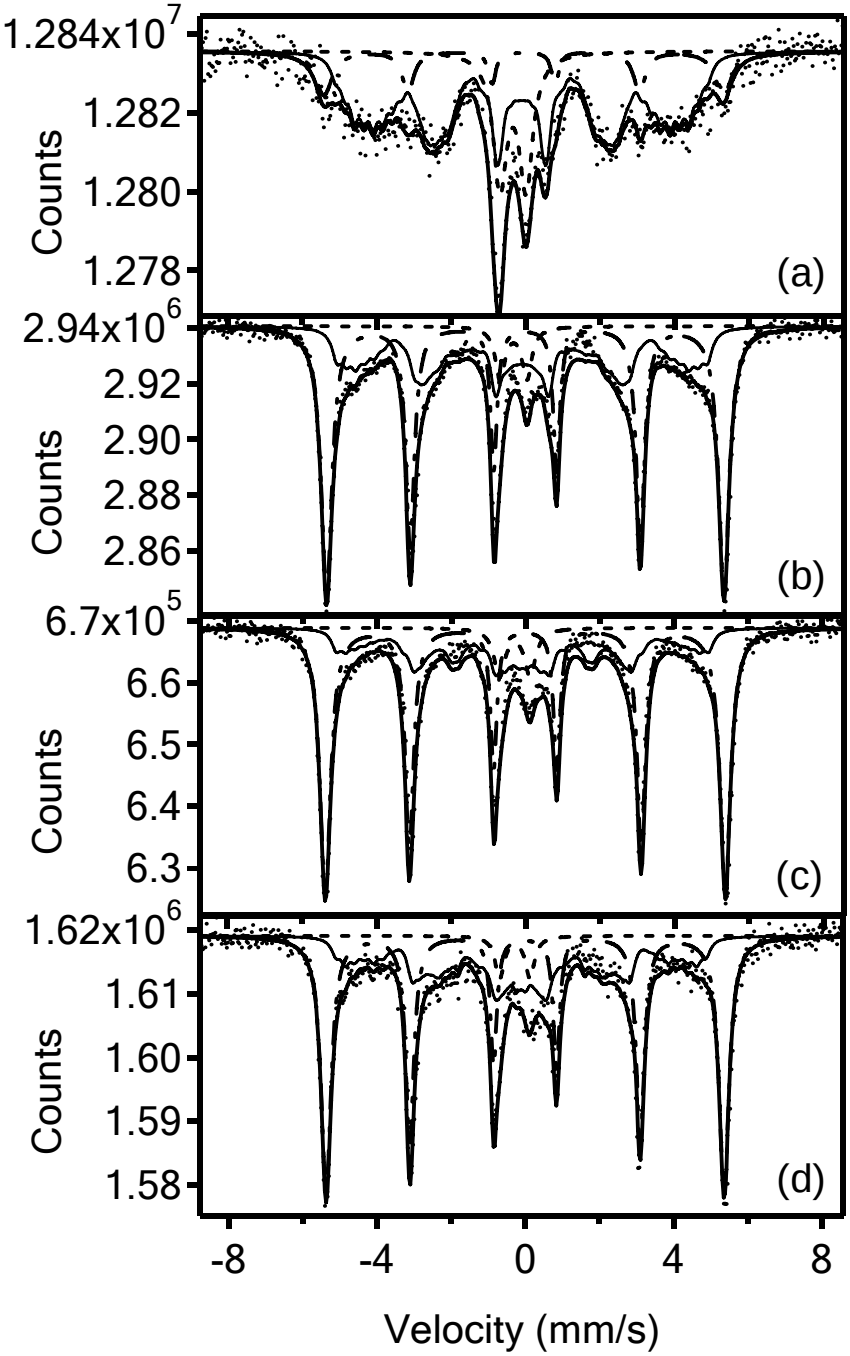
1.284x10^7
1.282
1.280
1.278
Counts
(a)
2.94x10^6
2.92
2.90
2.88
2.86
Counts
(b)
6.7x10^5
6.6
6.5
6.4
6.3
Counts
(c)
1.62x10^6
1.61
1.60
1.59
1.58
Counts
(d)
-8
-4
0
4
8
Velocity (mm/s)

Figure 2

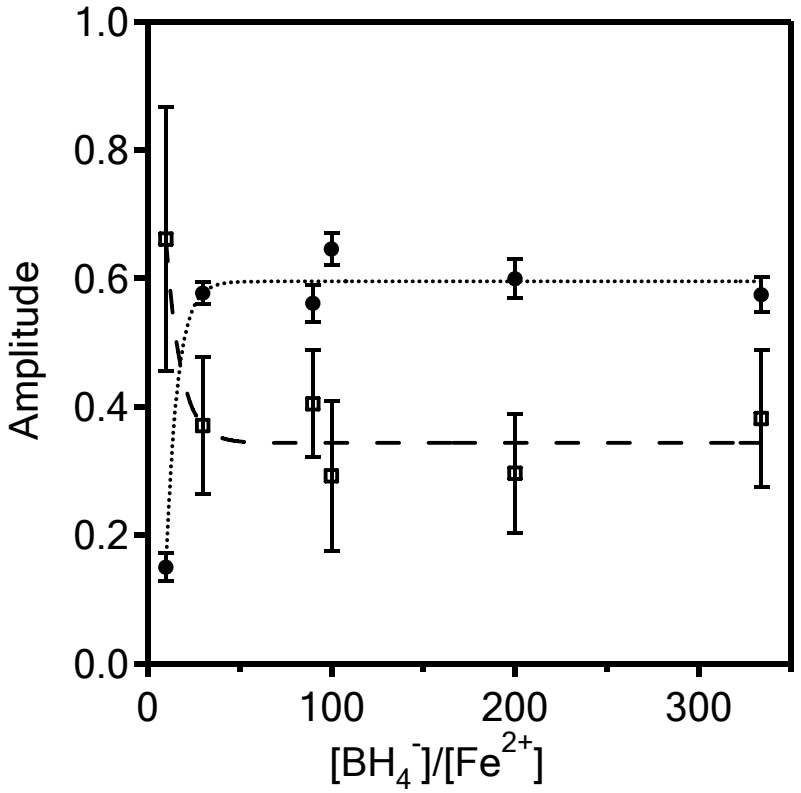

Figure 3

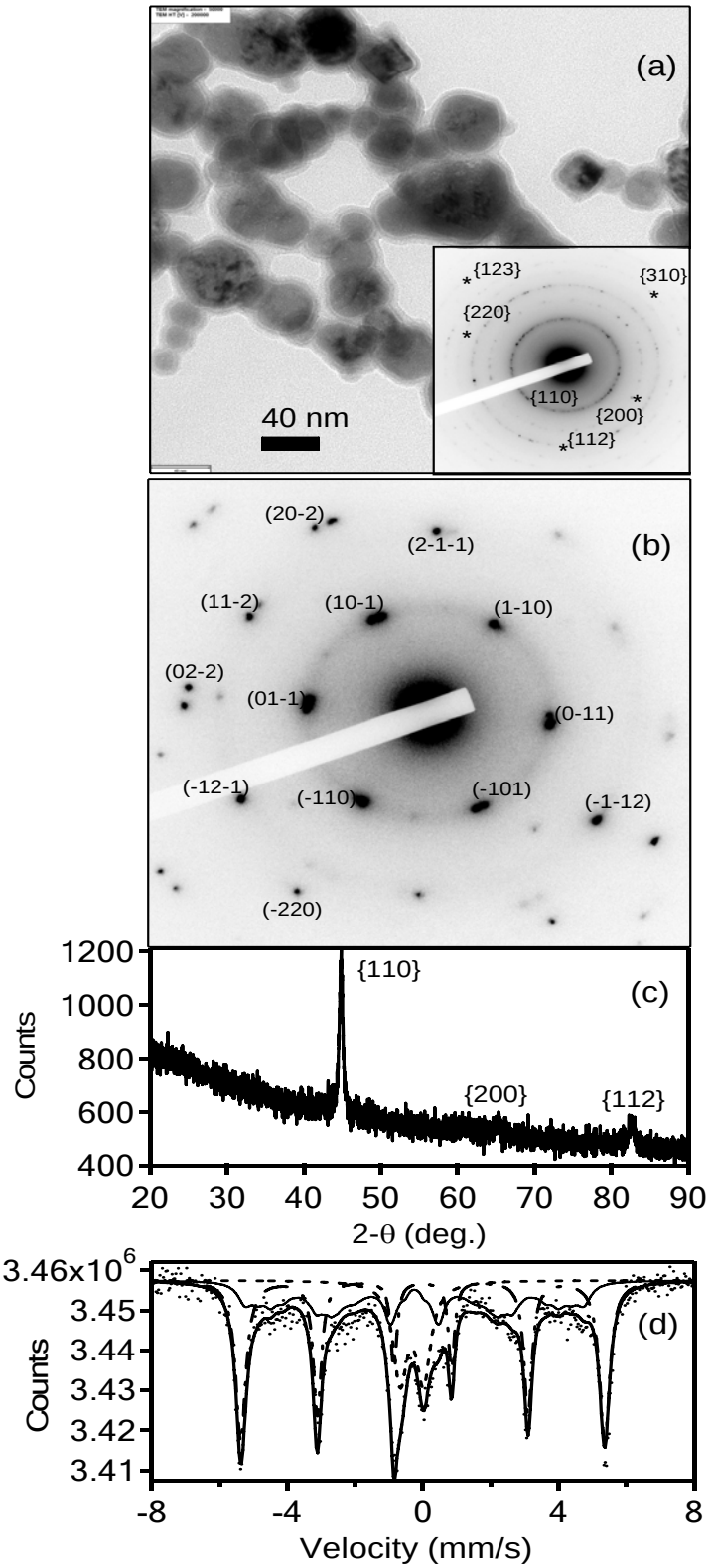
(a)
40 nm
{123}
{310}
{220}
{110}
{200}
{112}
(b)
(20-2)
(2-1-1)
(11-2)
(10-1)
(1-10)
(02-2)
(01-1)
(0-11)
(-12-1)
(-110)
(-101)
(-1-12)
(-220)
(c)
{110}
{200}
{112}
Counts
2-θ (deg.)
(d)
3.46x10^6
Counts
Velocity (mm/s)

Figure 4

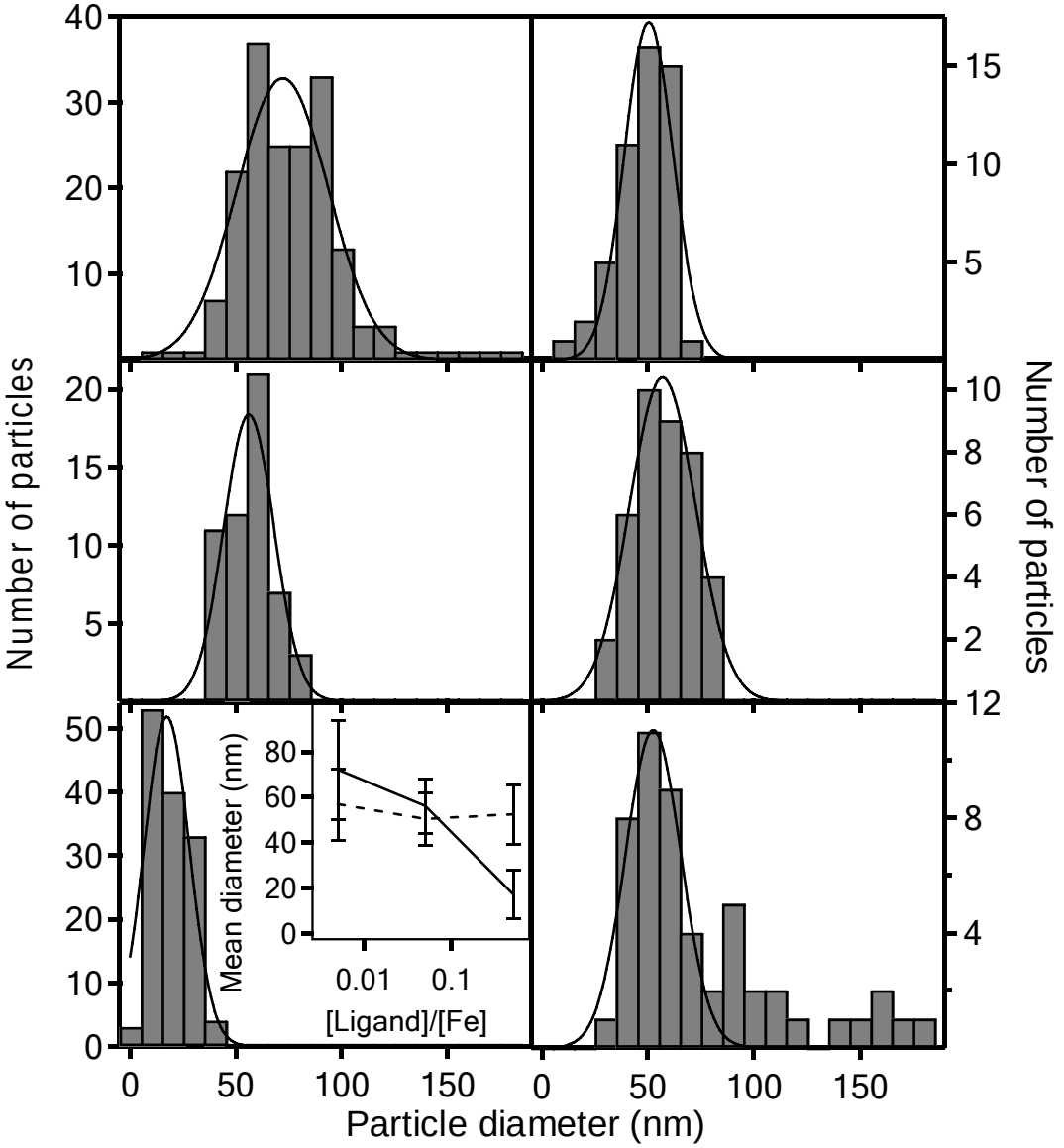
Number of particles
Number of particles
Particle diameter (nm)
Mean diameter (nm)
[Ligand]/[Fe]
0.01
0.1

Figure 5

C. To determine whether under what conditions can the magnetic nano particles be heated up to the desired temperatures.

To perform this part of the project, we first had to build a high frequency generator. Below, we see the circuit of the oscillator we built. It was designed to have a resonant frequency of about 121 kHz.

Induction Heater.

Frequency = 121 kHz

Voltage approximately = 30 volts

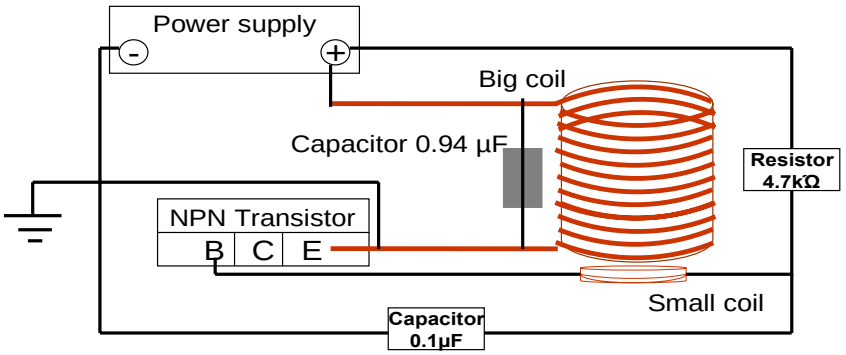

Diagram of the Induction Heater

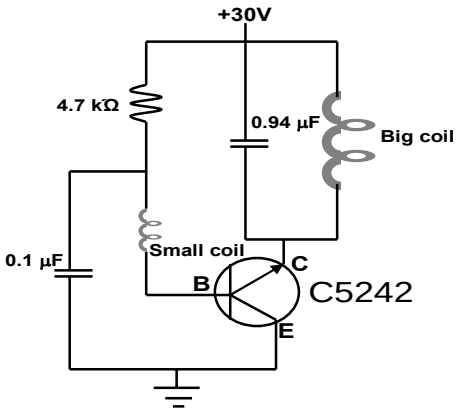

Schematic of the Circuit for the RF Induction Heater

Picture of the RF Induction Heater

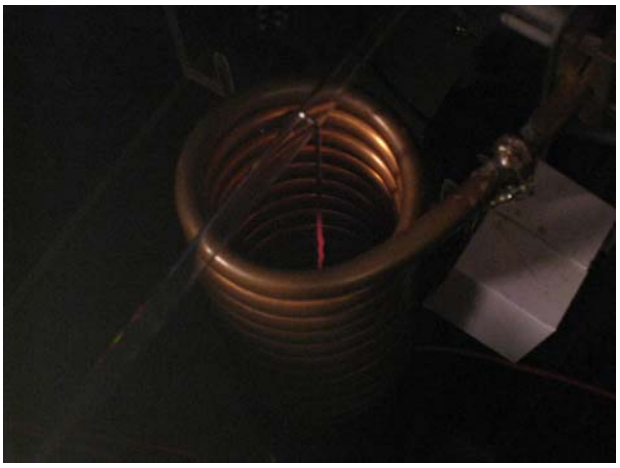

Image of a wire being heated up by the 121 kHz RF frequency

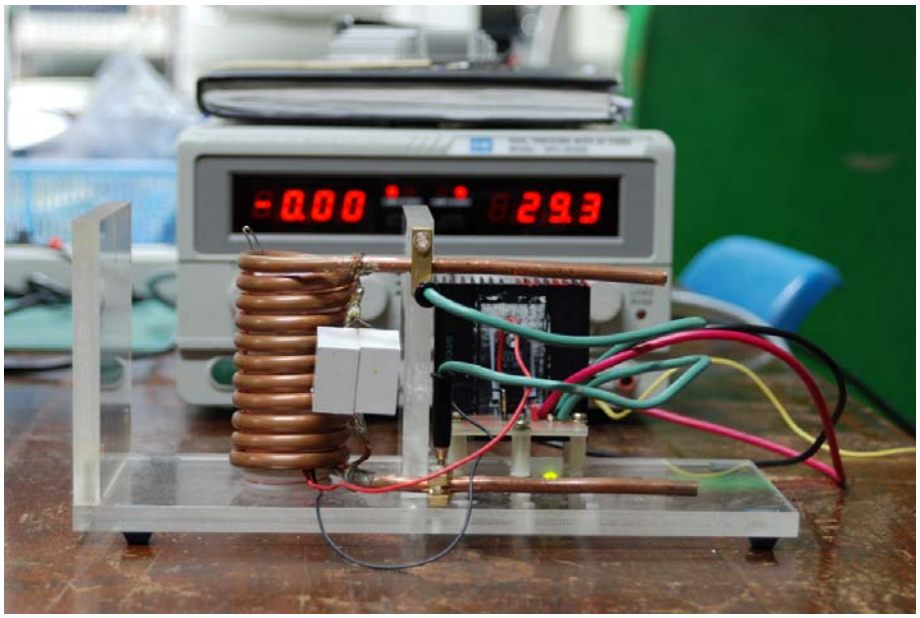

Overall Picture of the Induction Heater

Because the frequency of the RF was not high enough, the coil could not heat the magnetic nanoparticles. The frequency must be higher. We are now constructing new RF generator which can go up to 1 MHz. Therefore, this part of the project is not finished.

D. To see whether magnetic nano-particles can be moved in the blood into the vicinity of the tumor by placing strong magnets close to the tumor and whether they can be removed from the body by passing the blood through a shunt surrounded by a magnet.

To carry out this part of the research project, we fabricated some Silica coated $CoFe_2O_4$ nano particles using the method discussed in the next section. We have placed the coated magnetic particles at one end of a narrow class tube and observe

the nano particles migrate to the position where a magnetic nail is placed. In the proposal, we said that we were going to construct a mock body out of agar and demonstrate this movement. We still plan on doing this.

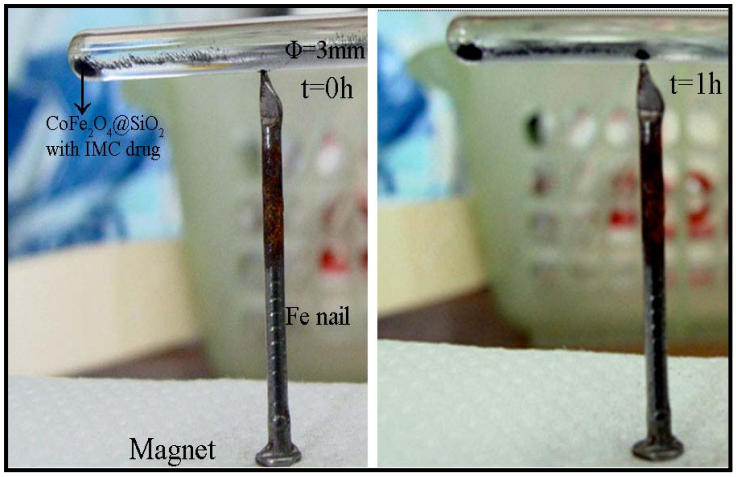

Movement of silica coated $CoFe_2O_4$ nano particles by the placement of a magnetized nail placed a distance away the original position of the nano particles

E. Formation of Silica Shell on Nano Spinel Ferrite Particles.

Hydroxyapatite (HAP) was prepared with $[NH_4]_2HPO_4$, $Ca(NO_3)_2 \cdot 4H_2O$ and NH_4OH obtained from UNIVAR (Australia). The chemical formula for the HAP is $Ca_{10}(PO_4)_6(OH)_2$. In this work, the concentration of reactants was fixed at a Ca/P ratio of 1.67. Each of constituents was dissolved in 50 ml of de-ionized water. The preparation steps were, first, adjust the pH of 50ml of the $[NH_4]_2HPO_4$ solution to 9.0 with NH_4OH. Next add the Ca solution and mix together. The pH of the resulting mixture is again adjusted to 9.0 by adding NH_4OH under constantly stirring. After stirring for several minutes, the clear aqueous solution of pH 9.0 is then placed in a conventional microwave oven operating in the frequency bands centered at 915 MHz. The reaction occurs under ambient air conditions while being irradiate for 20 seconds. The microwave irradiation accelerates the HAP particle growth. After cooling to room temperature, the precipitate particles are washed several times with de-ionized water of pH~7. The final powder products were obtained by freeze drying.

Cobalt ferrite nanoparticles were prepared using $Fe(NO_3)_3 \cdot 9H_2O$, $Co(NO_3)_2 \cdot 6H_2O$, NaOH from UNIVAR (Australia). Sodium dodecyl sulfate (SDS, Na_2SO_4) and ethylene glycol (EG) was from Fluka (Switzerland). In preparation of ferrite particles, the concentration ratio of Fe/Co was kept at 2:1 %mol and each chemical was dissolved in 25 ml de-ionized water and mixed together. The above solution was added to a solution of ethylene glycol (5ml) (3M) and Na_2SO_4 (3ml) (0.001M). The pH of the resulting $CoFe_2O_4$ precipitate was adjusted by adding NaOH under constant stirring and keeping the reaction at 60°C throughout. After adding NaOH in solution, formation of black particles of cobalt ferrite was noticeable. After completing the reaction, the samples were continuously stirred for 30 min and cobalt ferrite powder was obtained by filtration and addition of ethanol

followed by ultra-sonication for 30 min to separate aggregating particles. The powder products were obtained by drying in oven at 80°C overnight.

Hydroxyapatite (HAP) nanoparticles were synthesized by above technique. One gram of spherical HAP nanoparticles was dispersed in a mixture of ethanol and distilled water by ultra-sonication. Then 5 mL of cobalt magnetic fluid ($CoFe_2O_4$ nanoparticles dispersed in ethanol, 25 mg/mL) and 0.8 ml of TEOS in 50 mL of ammonium hydroxide were added into the suspension to reach a pH of ~11. The suspension was stirred for 4 hours at room temperature, and subsequently filtered and rinsed with distilled water and ethanol. The composite HAp and cobalt ferrite was then immersed in an acetic acid solution where the ratio of acid: H_2O equal to 1:10, pH = 2.5 for ~3 hours. The product was filtered and afterward, rinsed with distilled water to reach a pH of ~7 and dried at 60 °C overnight to yield magnetic $CoFe_2O_4$ encapsulated in silica nanospheres.

TEM of hydroxyapatite (HAp) nanoparticles synthesized by co-precipitation technique then heated at 500°C for 2 hours was shown in figure 1(a). The samples

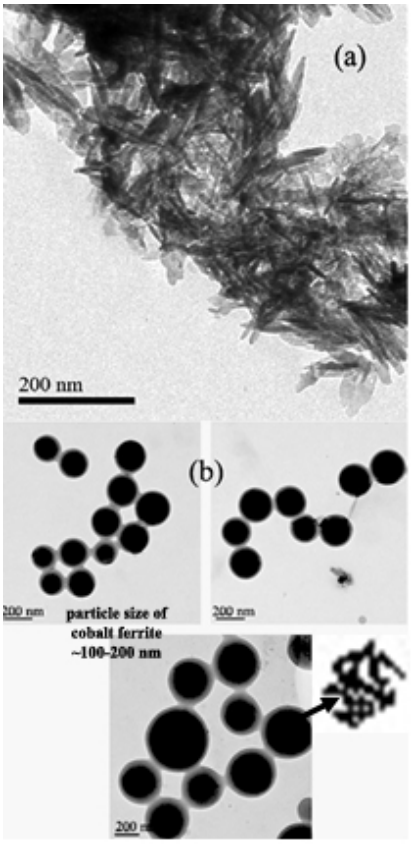

Figure 1. TEM micrograph of as-prepared hydroxyapatite (HAp) (a) and $CoFe_2O_4$ nanoparticles dispersed in ethanol (b).

have nano ribbon structure of 100 nm length and 20 nm width. The XRD patterns of prepared samples are shown in figure 2(a). They confirm the structure of hydroxyapatite because diffraction peaks occur at angles of 2θ~26°, 32°, 34°, 40°, 50°, 51°, 52° and 53°, which are typical for hydroxyapatite. Whereas, the synthesized cobalt ferrite nanoparticles had diffraction peaks at 30.2, 35.7, 43.6,

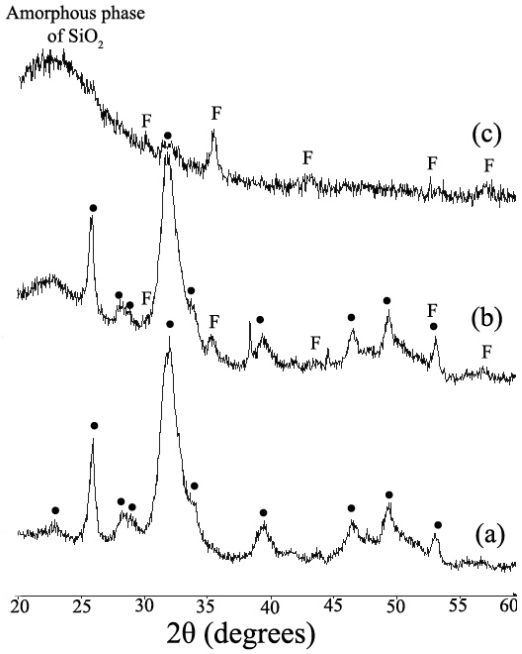

Figure 2. XRD patterns for hydroxyapatite (HAp) heated at 500°C/2hrs (a), mixed HAp and cobalt ferrite (b) and after composite materials HAp@$CoFe_2O_4$ aged in 1:10::nitric acid:deionized water for three hors (c).

53.6 and 57.3° which was related to $CoFe_2O_4$ nanoparticles. The TEM allowed measurement of particle size of cobalt ferrite (figure 1(b)) which exhibited sphere shape and had size of about 100-200 nm. Particularly, the TEM allowed viewing of particles having different forms such as chain form of cobalt nanoparticles which is attributed to the magnetic dipole–dipole interaction between neighboring particles. The most important property of nanoparticles is observed when the volume of the nanoparticles increases and the particles change from being superparamagnetic to ferromagnetic blocked (SP–FM). In the former state, the magnetization is oriented along the magnetic anisotropy axis, and in the latter state, the time average of the magnetization of the particle is zero. The anisotropic nature of the dipolar interaction in the formation of chains is favored, since the north and south poles of the dipolar nanomagnets attract each other while particles coming close to each other side by side with the parrallel magnetization direction will repel each other. During the synthesis, the suspension is stirred by a magnetic rod and a small magnetic field is present favoring the formation of chains. As a result of the dipolar interactions, the larger cobalt ferrite clusters form chains and sometimes closed loops in order to minimize the magnetostatic energy. The observed spontaneous self-assembly of the nanoparticles yields unique structures such as chains resembling sphere necklaces and loops demonstrating the importance of dipolar interactions even in wet-chemical synthesis.

XRD studies revealed the presence of hydroxyapatite (HAp) for samples prepared in figure 2(a). We also noted the presence of $CoFe_2O_4$ phase after mixing with HAp shown in figure 2(b). For XRD of the composite of HAp@$CoFe_2O_4$, reflection was extremely low in intensity in cobalt ferrite phase but reflections corresponding to hydroxyapatite remained highly intense. The strongest reflection

for the cobalt ferrite appeared when the samples were coated by SiO_2 then aged by acetic acid shown figure 2(c) corresponding to the diffraction pattern of $CoFe_2O_4$ at 30.2, 35.7, 43.6, 53.6 and 57.3° which is related to (220), (311), (400), (511) and (440) lattice planes, respectively [12]. However, after aging by acid the little amount of hydroxyaptite remaining was seen at 2θ~33 and confirmed by FT-IR reported later. In addition, the XRD patterns of SiO_2 coated ferrite shown in figure 2(c) contain reflections at 2θ~20°-28° attributed to amorphous SiO_2 phase.

The FT-IR spectra of cobalt ferrites encapsulated in silica matrix is shown in figures 3. A broad band attributed to surface absorbed water appears at 3416 cm^{-1}. The bands at 798 and 885 cm^{-1} are caused by vibrations (stretching) of the Fe^{3+}-Co^{2+} bonds when the Fe^{3+} ions are in the tetrahedral and octahedral crystal shapes of ferrite, respectively. These bands are not clearly observed and may be overlapped by Si bands. However, the intense bands in the HAP_ferrite spectra at 1088, 1035 and 961 cm^{-1} are due to the stretching mode in $(PO_4)^{-3}$ and the doublets at 602 and 562 cm^{-1} are due to the bending mode in $(PO_4)^{-3}$ which were absent when hydroxyapatite was removed after washing with acetic acid . The FT-IR spectra exhibit broad bands at 460, 800 and 1090 cm^{-1} characteristic of silica (SiO_2), with the most intense band due to symmetric stretching of the Si-O-Si chain. Other features are related to symmetric stretching of the Si-OH group (3400 cm^{-1}), symmetric stretching of Si-O-Si (800 cm^{-1}) and a bending vibration of the Si-O-Si chain (460 cm^{-1}). However, vibrational modes that could be attributed to a bonded silanol group, Si-OH (3200-3400 cm^{-1}) was not evident.

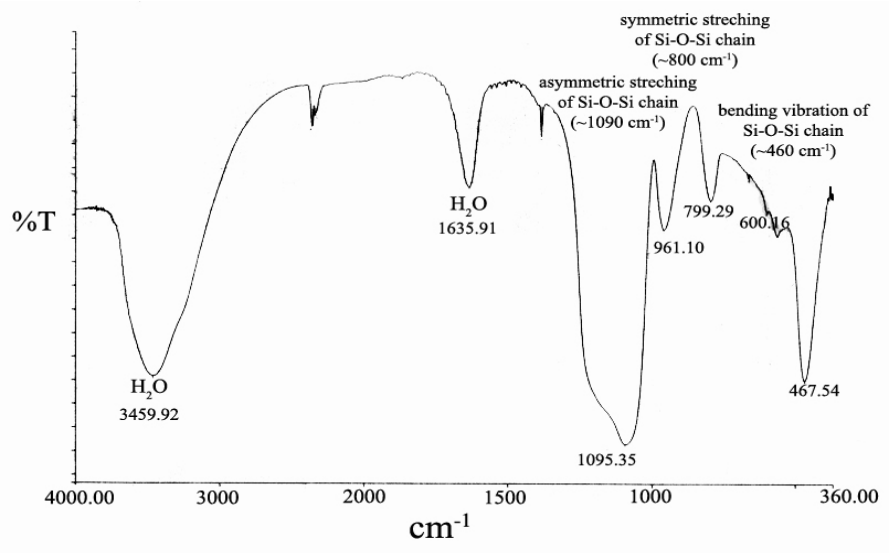

Figure 3. FT-IR spectra of synthesized $CoFe_2O_4$ nanoparticles were encapsulated in SiO_2 matrix.

Microstructure of the synthetic powders was observed by SEM. Figure 4(a) shows the SEM of composite hydroxyapatite with cobalt ferrite in low (left) and high (right) resolution. The powders of sizes between 0.2-0.5 μm can be observed. The size distribution appears to be uniform and less pore in the samples due to incorporation of $CoFe_2O_4$ in hydroxyapatite pores. Whereas, the morphology of

samples with coated with SiO_2 (figure 4(b)) are present as globular spheres of small particles less than 1 μm.

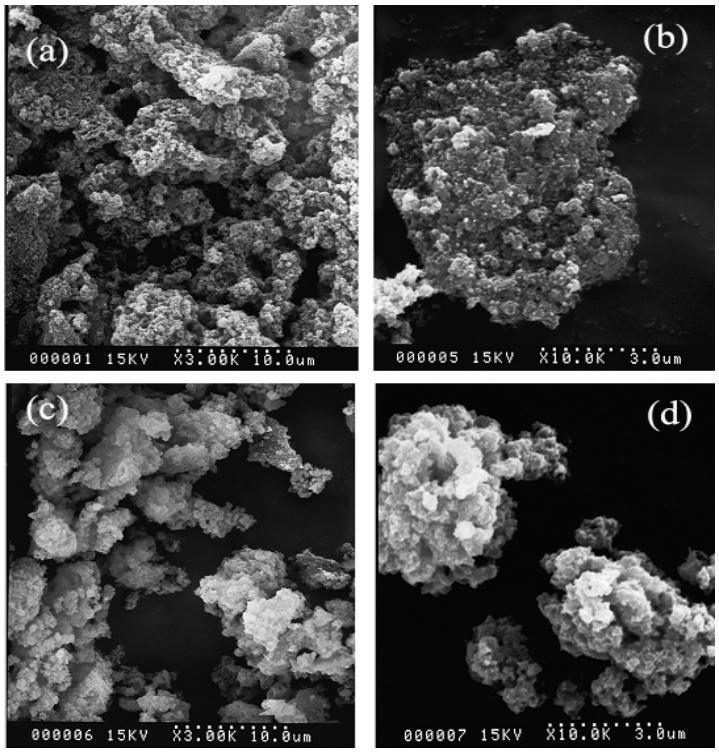

Figure 4. SEM image of the composite HAp@$CoFe_2O_4$ in low (left) and high (right) resolution (a) and after HAp@$CoFe_2O_4$ embedded in silica matrix then aged by nitric acid (b).

Figure 5(a) shows representative transmission electron micrographs (TEM) of ferrite nanoparticles attracted with hydroxyapatite (left hand) and the electron diffraction ring patterns of the nanoparticles HAp-Co ferrite (right hand), respectively. The TEM micrograph suggests that the $CoFe_2O_4$ nanoparticles were attracted to hydroxyapatite which is due to the accumulated particles on the ribbon structure of HAp. However, the distributions of accumulated cobalt ferrites are seen irregularly. The accumulated particles on HAp were confirmed by viewing the area's electron diffraction patterns which correspond to accumulated $CoFe_2O_4$ nanoparticles. This image contains the diffraction rings typical of a $CoFe_2O_4$ spinel structure, confirming the crystallinity of nanosized ferrites. The nanocrystallite size of the synthesized ferrites can also be determined from an analysis of the XRD pattern shown in figure 2. The XRD patterns exhibit broad diffraction peaks, indicating that the samples are made up of small crystals. The diffraction rings correspond to the reflection of the (1) (220), (2) (311), (3) (400) and (4) (440) planes. These correspond to the XRD peaks at $2\theta \sim 30.2°$, 35.7°, 43.6° and 53.6° in the XRD patterns shown in right hand of figure 5(a).

Agglomeration of cobalt ferrite magnetic nanoparticles coated with amorphous silica was observed by TEM in left hand of figure 5(b). The silica coating can be seen as inhomogeneous distribution of ferrite particles which corresponds to the distribution of particles in the preparation cobalt ferrite mixed with hydroxyapatite.

The composite nanoparticles formed have an average radius of 10-20 nm. In the right hand side of figure 5(b), the electron diffraction ring patterns of the nanoparticles Co ferrite-SiO_2 are shown. The pattern for the sample at the shell exhibits not well resolved ring spot due to the disordered nature of the sample typical of the amorphous SiO_2 phase.

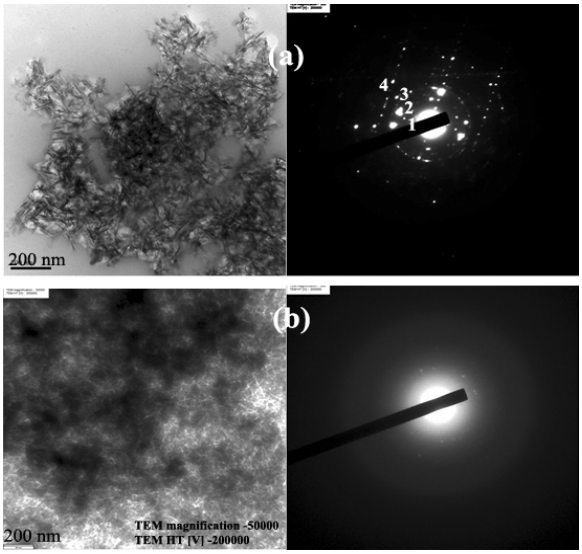

Figure 5. TEM images of (a) SiO_2@Co-ferrite and **Electron diffraction rings** fabricated at 200 keV of the nano sized SiO_2@Co-ferrite particles (b), (1) (220), (2) (311), (3) (400) and (4) (440) planes.

The electron spin resonance (ESR) at room temperature of HAp-cobalt ferrite and cobalt ferrite –silica are displayed in figure 6(a) and 6(b). The spectra show a broad peak at g≈2.01 with peak to peak linewidth ≈1145 and 908 gauss for HAp and silica cobalt ferrite, respectively. The peak at g-factor equal to 2.01 rises from the

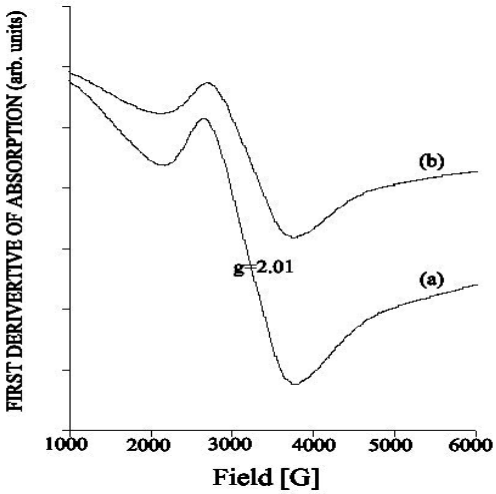

Figure 6. Electron spin resonance (ESR) of hydroxyapatite_Co ferrite (a) and SiO_2_Co ferrite (b) recorded at room temperature

ferrite particles located on the surface or from the oxide ion particles such as FeOOH complexes where the iron and cobalt ions interact with each other. However, in this work no significant observation of the resonance peak at g-factor at 4.23 was made indicating during the mixing of $CoFe_2O_4$ and hydroxyapatite, the isolated paramagnetic Fe^{3+} ion was probably not substituting into Ca^{2+} sites in the hydroxyapatite lattice. Broad resonance lines at $g \cong 2.0$ are frequently observed in the ESR spectra of superparamagnetic and ferromagnetic iron-cobalt nano particles. Although, the cobalt ferrite composite with silica was aged by acetic acid the magnetic properties of $CoFe_2O_4@SiO_2$ still remain. This result suggests that magnetic particles after embedded in acid solution did not decompose but the ESR intensity decreased due to some cobalt ferrites that dissolved in acid.

Appendix A

Publications 2008/2009

1. B. Soodchomshom, I.M. Tang, R. Hoonsawat, *"The Critical Josephson currents MgB_2/normal-metal/MgB_2 Tunnel Junction: Bogoliubov-de Gennes Approach"* Physica C **468,** 47 (2008).

2. W. Pon-On, P. Winotai, I.M. Tang, "*Nanocrystallization kinetics of amorphous magnetic ribbons $Fe_{81}B_{13.5}Si_{3.5}C_2$',* Mat. Res. Bull. (2008) **43**, 1004 (2008).

3. W. Pon-On, S. Meejoo, I.M. Tang, "Substitution of Manganese and Iron in Hydroxyapatite: Core/Shell Nanoparticles.", Mat. Res. Bull.**43**, 2137 (2008).

4. C. Saiyasombat, N. Petchsang, I.M. Tang, J.H. Hodak, "*Preparation of iron boride-silica core-shell nanoparticles with soft ferromagnetic properties"*. Nanotechnology **19**(8), 085705 (2008). .

5. Jirasak Wong-ekkabut, Svetlana Baoukina,Wannapong Triampo, I-Ming Tang, D. Peter Tieleman, Luca Monticelli "*A simulation study of fullerene translocation through lipid bilayers* " Nature Nanotechnology **3**, 363 (2008).

6. B. Soodchomshom, I.M. Tang, R. Hoonsawat, "*Quantum transport of injected electrons in an asymmetric FM/I_1/SC/I_2/FM junction: Directional dependence."* Physica C **468**, 1006 (2008).

7. B. Soodchomshom, I.M. Tang, R. Hoonsawat, *"Quantm modulation effect in a graphene based magnetic tunnel junction."* Phys. Lett. A **372**, 5054 (2008).

8. W. Pon-on, S. Meejoo, I.M. Tang, "Formation *of hydroxyapatite crystallites using organic template of polyvinyl acholol dodecyl sulfte (SDS)."* Mat. Chem. Phys. **112**, 452 (2008) .

9. B. Soodchomshom, I.M. Tang, R. Hoonsawat, *"Josephson current in a graphene SG/Ferromagnetic Barrie/SG junction*", Physica C **468**, 2301 (2008).

10. B. Soodchomshom, I.M. Tang, R. Hoonsawat, *"Dirac quasi particle tunneling in a SG/ferromagnetc barrier/SG graphene junction*", Physica C **468**, 2361 (2008).

11. P. Pungsumpun, I.M. Tang, "*Transmission Model for* Plasmodium Vivax M*alaria: Conditions for Bifurcation".* Int. J. Biomed. Sci. **3** (3), 161 (2008).

12. P. Nalakarn, I.M. Tang, W. Triampo, "*Fractal studies on the spatial patterns of trees: A case study in Khao Yai National Park, Thailand".* ScienceAsia **34**. 409 (2008).

13. R. Kongnuy, P. Pongsumpun, I.M. Tang, *"Analysis of a MathematicalModel for Dengue Disease in Pregnant Cases",* Int. J. Biomed. Sci. **3** (3), 192 (2008).

14. P. Pungsumpun, I.M. Tang, "*Mathemtical Model for the Transmission of* P. Falcoparum *and* P. Vivax *malaria along the Thai-Myanmar Border"***.** Int. J. Biomed. Sci. **3** (3), 200 (2008).

15. P. Pungsumpun, I.M. Tang, *"Effect of the Seasonal Variation in the Extrinsic Incubation Periao on trhe Long Term Behavior of the Dengue Hemorrhagic Fever Epidemic",* Int. J. Biomed. Sci. **3** (3), 209(2008).

16. K. Patanarapelet, I.M. Tang, "*Effect of Time Delay on the Transmission of Dengue Fever"***.** Intern. J. Med. Biomed. Sci. **3** (4), 239 (2008).

17. S. Sarakorn, I.M. Tang, "*No one set of parameter values can simulate the epidemics due to SARS occurring at different localities."* Intern. J. Med. Biomed. Sci. **3** (4), 249 (2008).

18. W. Jumpen, B. Wiwatanapataphee, Y.H. Wu, I.M. Tang, *"A SEIQR Model for Pandemic Influenza and its Parameter Identification"***.** Intern. J. Pure Appl. Math. **52** (2), 247 (2009).

19. B. Soodchomshom, I.M. Tang, R. Hoonsawat, "*Dirac supercurrent in an asymmetric grqphene-based* $SG_1/N_B/SG_2$ *junction.*", Physica C **469**, 157 (2009).

20. N. Petchsang, W. Pon-On, J.H. Hodak, I.M. Tang, "*Magnetnic Properties of Co-Ferrite Nano-particles having a Core/Shell Structure."* J. Mag. Magn. Mat. **321**, 1990 (2009).

21. R. Kongnuy, P. Pongsumpun, I.M. Tang, *"Mathematical Model for Dengue Disease with Maternal Antibodies",* Int. J. Biol Med. Sci. **5** (1), 5 (2009).

22. S. Krobthong, S. Jullanope, I.M. Tang, "*Role of the Interlayer Copling in the Cuprate High* T_c *Superconductor."* ScienceAsia **35**, 64 (2009).

23. B. Soodchomshom, I.M. Tang, R. Hoonsawat, "*Dirac tunneling magneto resistance in a double ferromagnetc graphene structure*", Physica E **41**, 1310 (2009).

24. B. Soodchomshom, I.M. Tang, R. Hoonsawat, *"Dirac quasi particle tunneling in a NG /ferromagnetc barrier/SG graphene junction*", Physica C **469**, 689 (2009).

25. B. Soodchomshom, I.M. Tang, R. Hoonsawat, *"Massive Dirac Fermion Transport in a Gapped*
Graphene Based magnetic Tunnel Junction."**,** Physica E **41**, 1475 (2009).

26. B. Soodchomshom, I.M. Tang, R. Hoonsawat*, "Josephson effects in* MgB_2*/Thin Insulator/*MgB_2 *TunnelJunction",* Sol. State Commun. **149**, 1012 (2009).

27. W. Pon-On, P. Winotai, I.M. Tang, *"Ferromagnetic Resonance Study of Amorphous and Nano-*
Crystalline $Fe_{81}Fe_{13.5}S_{3.5}B_2$ *Ribbons"*, Int. J. Mod. Phys. B **23**, 3391 (2009).

28. B. Soodchomshom, I.M. Tang, R. Hoonsawat, "*Tunneling Conductance in a Gapped Graphene-Based Superconducting Structure: Case of Massive Dirac Electrons."* Phys. Lett. A (2009)